Journal Name

ARTICLE TYPE

Cite this: DOI: 10.1039/xxxxxxxxxx

Femtosecond Time-Resolved Photoelectron Spectroscopy of the Benzyl Radical†

A. Röder[a,b,c], A. Humeniuk[a,c], J. Giegerich[a], I. Fischer[a], L. Poisson[b] and R. Mitrić[a]

Received Date
Accepted Date

DOI: 10.1039/xxxxxxxxxx

www.rsc.org/journalname

We present a joint experimental and computational study of the nonradiative deactivation of the benzyl radical, C_7H_7 after UV excitation. Femtosecond time-resolved photoelectron imaging was applied to investigate the photodynamics of the radical. The experiments were accompanied by excited state dynamics simulations using surface hopping. Benzyl has been excited at 265 nm into the D-band ($\pi\pi^*$) and the dynamics was probed using probe wavelengths of 398 nm or 798 nm. With 398 nm probe a single time constant of around 70-80 fs was observed. When the dynamics was probed at 798 nm, a second time constant τ_2=1.5 ps was visible. It is assigned to further non-radiative deactivation to the lower-lying D_1/D_2 states.

1 Introduction

Benzyl is the prototype of a resonance-stabilised radical with a π-electron system.[1] As the primary unimolecular reaction product of toluene[2] it is of considerable interest in combustion chemistry, because toluene itself is a common fuel additive and considered to be a model for the combustion of aromatic fuels.[3] Due to the relatively high stability of the benzyl radical, a comparably long lifetime in a reactive environment can be expected and knowledge on the benzyl dynamics and kinetics is considered relevant for understanding its combustion chemistry. Therefore a number of previous studies focused on the kinetics of hot benzyl reactions in order to determine rate constants for high-temperature reactions.[4–7] In all these experiments benzyl was excited at 266 nm. It was assumed that the radical deactivates by a rapid internal conversion to the electronic ground state, forming internally hot ground state radicals, which subsequently react. However, the details of the deactivation after UV excitation, although relevant for all experiments that employ optically excited benzyl, are not yet understood. We therefore initiated a new study of the UV band using photoelectron imaging as the probe method and accompanied it by molecular dynamics simulations to provide a solid understanding of the photodynamics.

The relevant electronic states are given in Figure 1. An ionization energy of 7.249 eV was determined by zero kinetic energy photoelectron (ZEKE-) spectroscopy.[8] This is in good agreement with the ionization energy of 7.252(5) eV determined recently via threshold photoelectron spectroscopy.[9] The two lowest electronically excited states of the neutral, A and B, have been studied in some detail by laser-induced fluorescence,[10,11] multiphoton ionization[12] and cavity ringdown spectroscopy[13] and were shown to be vibronically coupled. Rotational resolution was achieved, indicating a long lifetime. The C-state was investigated by absorption spectroscopy in a gas cell[14] and by emission spectroscopy in a 77 K cyclohexane matrix. The C-state was assumed to have $^2A_2$ symmetry,[15] but in the following we will show that this assignment has to be revised. Recently we studied this state by time-resolved photoionization and found a two-step deactivation. For the origin band time constants of 400 fs and 4.5 ps were determined and assigned to a step-wise deactivation by internal conversion to D_0[16]. In a previous time-resolved photoionization study at 255 nm excitation a lifetime of approximately 150 fs was found.[17] Earlier work assigned this band, which maximizes around 253 nm, to the D $^2B_2$ state.[4,5] Again we will revise this previous assignment below. Irradiation at 266 nm is assumed to excite the red edge of this band. Zhang and coworkers investigated the photodissociation dynamics of benzyl by H-atom Rydberg time-of-flight spectroscopy and concluded that it dissociates to fulvenallene in a statistical fashion after rapid internal conversion to the electronic ground state.[18] Fulvenallene was also suggested to be the main dissociation product by *ab initio* computations.[19] As shown by various groups, photoelectron detection provides a more detailed insight into the intramolecular dynamics than simple ion detection.[20–23] Therefore we chose this approach in the present study. Only few reactive molecules have yet been studied using this method.[24–26] For our study we chose an excitation wavelength of 265 nm for best comparison with the large number of

[a] *Institute of Physical and Theoretical Chemistry, University of Würzburg, Am Hubland, D-97074 Würzburg; e-mail: ingo.fischer@uni-wuerzburg.de, roland.mitric@uni-wuerzburg.de*

[b] *LIDYL, CEA, CNRS, Université Paris-Saclay, CEA Saclay 91191 Gif-sur-Yvette France; e-mail: lionel.poisson@cea.fr*

[c] These authors contributed equally to this work.

† Electronic Supplementary Information (ESI) available: [additional computational information]. See DOI: 10.1039/b000000x/

previous data recorded at 266 nm excitation.[4–7] The experiments

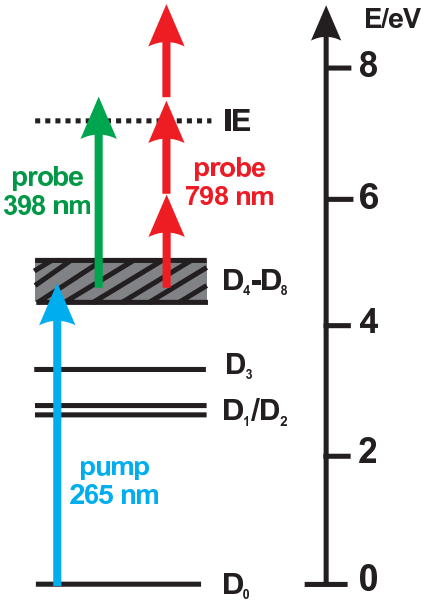

Fig. 1 Energy diagram depicting the relevant electronic states of benzyl based on computations. The pump/probe schemes employed in the experiment are indicated by arrows. Around 5 eV several states lie very close in energy.

are accompanied by computations to gain a deeper insight into the molecular mechanism underlying the excited state deactivation of benzyl. The simulation of coupled electron-nuclear dynamics "on the fly" in the framework of Tully's surface hopping method[27] showed to be a successful approach and yields the electronic states involved in the dynamics as well as the time scales for the various steps. The combination of gas phase spectroscopy and trajectory calculations has been successfully applied to unravel the photodynamics of cyclopropenylidene[24,28], propargylene[29] and recently the 2-methyl allyl radical[30].

2 Experimental Methods

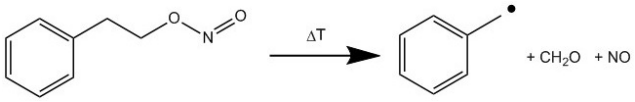

Fig. 2 The reaction scheme for the generation of benzyl radical by pyrolysis of 2-phenylethylnitrite.

A free jet of benzyl radicals was generated by a supersonic flash pyrolysis[31] of 2-phenylethylnitrite according to the reaction scheme presented in Figure 2. 2-phenylethylnitrite was synthesized from 2-phenylethanol following the procedure given for other nitrites.[32] All chemicals were purchased from Sigma-Aldrich and used without further purification. The precursor vapour was entrained at room temperature in 1 bar of argon and expanded through a short, heated silicon carbide (SiC) tube attached to a water-cooled solenoid pulsed valve operating at 20 Hz. Cooling the pulsed solenoid valve guaranteed a stable operation of the valve and suppressed decomposition of the precursor before passing through the SiC tube. The jet expanded into the source chamber, passed a 1-mm skimmer and reached the detection chamber, equipped with a time-of-flight spectrometer (TOF-MS) and a VMI detector capable of mapping ion or electron kinetic energy distributions.[33] Typical operating pressures in the source and detection chamber were 5 x 10^{-5} mbar and 4 x 10^{-7} mbar respectively. The femtosecond laser source of the LUCA/SLIC femtosecond laser facility of Saclay was used to perform the pump (265 nm) - probe (798/398 nm) experiments. The laser system consists of a 20 Hz femtosecond Ti:Sa oscillator/amplifier system as described previously.[34] The 3^{rd} harmonic of the Ti:Sa at 265 nm (10-50 μJ) was used as the pump pulse. The photoexcited radicals were probed with either the fundamental (between 796 and 798 nm, 100-700 μJ) or the second harmonic (around 398 nm, 50-100 μJ) of the Ti:Sa laser. Pump and probe beam were overlapped in a small angle. Both beams were focused several centimeters away from the interaction region, the pump beam by a 700 mm lens; the probe beam using a 500 mm lens, to reduce one-colour background signals. In the delay scans the probe pulse was delayed with respect to the pump pulse via a computer-controlled stepper motor. The time intervals between two data points in a delay scan were varying, with time intervals of 2 fs near the time origin and intervals of 1.5 ps at the end of a delay scan. Each spectrum was obtained as an average over 5 to 6 individual delay scans. Within one scan the ion signal as well as the PE images were integrated over 150 laser shots. The probe beam was polarized horizontally, the polarisation of the pump laser was turned from parallel to orthogonal using a $\lambda/2$ waveplate. No dependence on the relative polarization of pump and probe pulse was observed, therefore the rotational mean is discussed in the experimental spectra. The one-colour background signal was subtracted from the delay traces. The PE spectra were treated with the pBASEX algorithm[35] to reconstruct the 3D features of the electron sphere and to allow separating the polarised and unpolarised part of the image.

3 Computational Methods

In order to identify and characterize electronically excited states of the benzyl radical we have performed calculations employing a hierarchy of quantum-chemical methods with increasing accuracy including TDDFT, EOM-CCSD and CASSCF+MRCI. Time-dependent density functional theory TD-DFT calculations were performed using the Gaussian program package[36] and employing the PBE[37], PBE0[38], LC[39]-PBE, B3LYP[40,41], CAM-B3LYP[42] and ωB97X[43] functionals combined with the aug-cc-pVDZ basis set. As can be seen from the TDDFT results presented in the supplementary material, all density functionals fail to correctly represent the order or energetic separation of the relevant excited states, which can be attributed mostly to spin contamination. In order to identify and assign the electronically excited states as well as to construct the optimal active space needed to carry out dynamics simulations, we have first performed CASSCF+MRCI benchmark calculations. The benzyl radical has 49 electrons, 7 of them participate in the π-system. The active space relevant for the lowest few excited states consists of the 7 π-orbitals (3 doubly occupied, 1 singly occupied and 3 unoccupied), a low-lying s-Rydberg orbital and 3 p-Rydberg orbitals (cf. Fig. 3). The

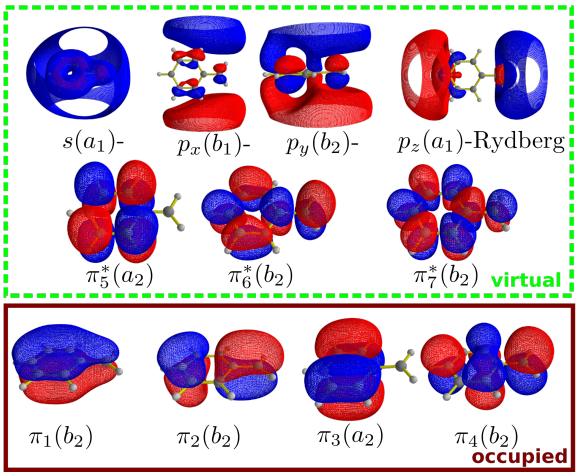

Fig. 3 Benzyl radical, relevant valence orbitals, CASSCF/(aug-cc-pVDZ, s-,p-Ryd). The C_{2v} irreducible representations are given in brackets.

p_y-Rydberg orbital is perpendicular to the molecular plane and lies higher in energy than the p_x- and p_z-Rydberg orbitals. State-averaged CASSCF followed by the MRCI treatment of the dynamic correlation were performed using the aug-cc-pVDZ and 6-31 G* basis sets which have been augmented by functions optimized for the description of s- and p-Rydberg states. The Rydberg basis functions have been computed according to the recipe developed by Kaufmann et al.[44] and were centered at the carbon atom C_1 that is bound to the -CH_2 group. Notice that the exact positioning of the center of Rydberg orbital is not critical as it extends over the entire molecule. SA-CASSCF calculations have been performed by giving all states equal weights and the orbitals and the configuration coefficients were optimized simultaneously, starting with the properly reordered RHF orbitals as initial guess. Important points on the potential energy surface were subsequently characterized using the SA-5-CASSCF/(7,8)/(6-31G*,s-Rydberg) method. The conical intersections were optimized using Molpro's conical program[45] taking the Franck-Condon point as the initial geometry.

A script for generating the exponents of the Rydberg basis functions and a complete MOLPRO input for the MRCI calculation are listed in the supplementary material.

The photodynamics of the benzyl radical was simulated using the surface hopping method coupled to CASSCF(7,8) with the (6-31G*, s-Rydberg) basis set, which provides reasonable balance between the computational accuracy and efficiency needed to carry out direct dynamics. 100 trajectories were lifted vertically to the $2\,^2A_2$ ($\pi-\pi^*$)-state and were propagated for 1 ps. For the inital conditions the geometry of the benzyl radical was optimized at the PBE/6-311++G**[46] level of theory. A subsequent frequency calculation provided the normal modes needed for constructing the Wigner distribution in the harmonic approximation. 100 initial conditions (nuclear positions and momenta) were sampled randomly from the Wigner distribution and were equilibrated on the ground state at a constant temperature of $T = 50$ K. Newton's equations for the motion of the nuclei were integrated with a time step of 0.1 fs. The electronic amplitudes, that determine the hopping probabilities according to an improved version[47] of Tully's surface hopping scheme[48], were integrated in the local diabatic basis[49] with a time step of $4 \cdot 10^{-5}$ fs. Scalar non-adiabatic couplings were computed from the wavefunction overlaps between consecutive time steps[50].

4 Results

4.1 Mass Spectra

Experiments on reactive molecules require an identification of all species that contribute to the time-dependent signals. Thus we first optimized the pyrolysis conditions by photoionization mass spectrometry. Typical mass spectra with pyrolysis present are given in Figure 4. The pump- and probe beam were attenuated to minimise one-colour signals. An intense benzyl signal appears at m/z = 91 and a small signal at m/z=65 is the only apparent side product from pyrolysis. As visible, the 265 nm pump beam produces a non-negligible background signal due to two-photon ionization, in contrast to the probe beam. However, the two-color pump-probe signal around t0 is larger by a factor of four at the zero in time.

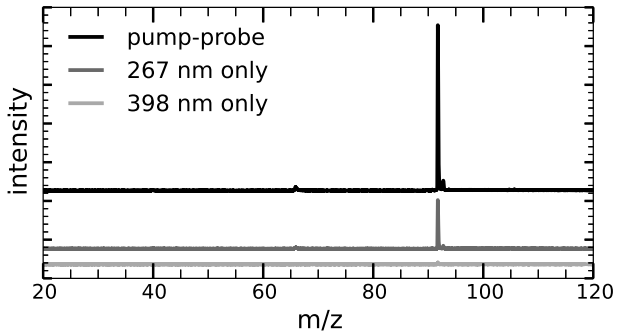

Fig. 4 Mass spectra of the benzyl radical, produced via pyrolysis, recorded at zero time delay between pump and probe laser (265+398 nm, top black trace). A strong signal from the radical (m/z=91) as well as a small fragment ion peak (loss of ethylene, m/z=65) is detected. The signal at m/z=92 is due to the ^{13}C satellite of benzyl. The one-colour background signal for the pump-only case (centre dark grey trace) is small and negligible for the probe-only case (bottom light grey trace).

4.2 Time-resolved Photoelectron Spectra, TR-PES

As mentioned above TR-PES provides more insight into the excited state dynamics than photoionization mass spectrometry. Since the mass spectra (cf. Figure 4) show no significant side product, we base our analysis of the dynamics on TR-PES, using photoelectron imaging detection. Spectra were recorded at two different probe wavelengths, 398 nm, depicted in Figure 5 and 798 nm, see Figure 6. While one-photon ionization is accomplished at 398 nm, at least two photons are required at 798 nm. In both spectra the photoelectron intensity is displayed as a function of the electron kinetic energy (eKe, vertical axis) and of the time delay (horizontal axis). The experimental data were fitted assuming a sequential model, applying the expressions described in a previous publication.[51] The time constants were convoluted with the instrument response function (IRF). The maximum eKE possible for a given multiphoton process [1+m'] is indicated in

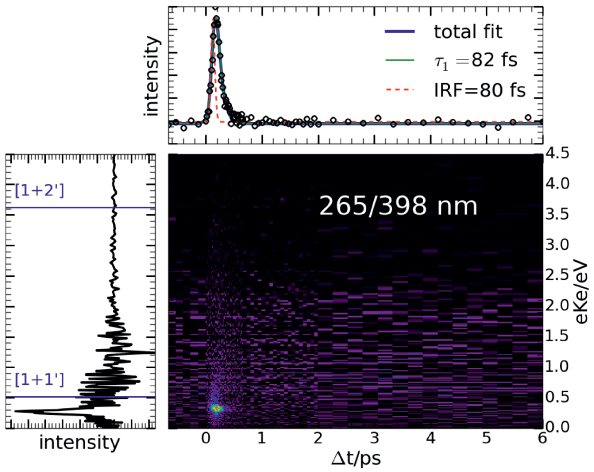

Fig. 5 TRPES with 265 nm pump/398 nm probe. The time-dependence of the total photoelectron signal (top trace) can be fitted with a single time constant τ_1=82 fs. The graph on the left shows the photoelectron kinetic energy summed over all delay times. The pump only/probe only signal was subtracted from the whole signal.

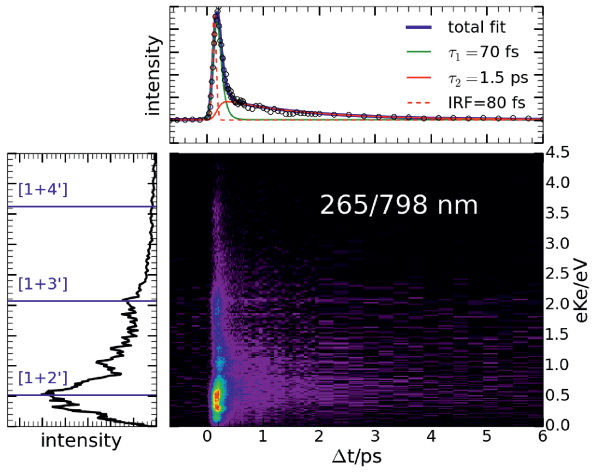

Fig. 6 TRPES with 265 nm pump/798 nm probe. The time-dependence of the total photoelectron signal (top trace)can be fitted with two time constants, τ_1=70 fs and τ_2=1.5 ps. The graph on the left shows the photoelectron kinetic energy summed over all delay times. The pump only/probe only signal was subtracted from the whole signal.

the Figures for various values of m. The first triplet state $\tilde{a}^{+3}B_2$ and the first singlet state $\tilde{A}^{+1}B_2$ in the benzylium cation are at 9.180 and 9.62 eV respectively[9], and can only be reached via a [1+2']-process. This would result in a maximal excess energy of 1.73 and 1.29 eV for $\tilde{a}^{+3}B_2$ and $\tilde{A}^{+1}B_2$ respectively, but no bands are observed in this energetic region. The spectrum recorded at 398 nm probe is dominated by a single band at low eKE, which corresponds to one-photon ionization into the ground state of the ion. This indicates diagonal Franck-Condon factors in the probe step. The band shows a fast monoexponential decay with a time constant τ_1 = 82 fs. The signal at larger eKE on the other hand is negligibly small.

On the other hand the TR-PE spectrum recorded at λ_{probe}=798 nm is markedly different from the one obtained at λ_{probe}=398 nm. Along the eKE axis a broad band is visible that shows a series of individual peaks. The peak observed at 398 nm appears again at eKE ≈ 0.3 eV and corresponds to [1+2'] two-photon ionization into the ionic ground state. The first triplet state $\tilde{a}^{+3}B_2$ in the benzylium cation can now be ionized in a [1+3']-process, which results in an maximal excess energy of 0.16 eV. This may correspond to the shoulder on the lower-energetic side of the peak at eKE≈ 0.3 eV. Another probe photon is necessary to excite into the first singlet excited state $\tilde{A}^{+1}B_2$ of the benzylium cation in a [1+4']-process, leading to a maximal excess energy of 1.27 eV. No pronounced peak is observed in this energy region. As can be seen in Figure 7, the peak at 0.3 eV dominates the first 60 fs (black trace). At later times the band at eKE ≈ 1.0 eV gains in intensity relative to the first peak. This change of the PE-spectrum indicates a non-radiative deactivation into a different electronic state, as has been outlined in the literature.[52] The series of peaks converging onto 1.56 eV, the energy of a single probe photon, do not match bands in the photoelectron spectrum of benzyl and are thus likely caused by intermediate Rydberg state resonances of

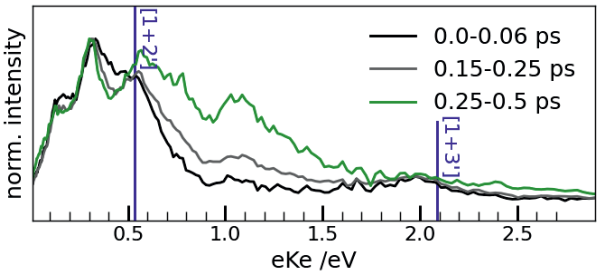

Fig. 7 Selected traces of the TRPES spectrum with 265 nm pump/798 nm probe (see fig. 6). The traces are normalized each on the maximum.

benzyl. They are excited by two 798 nm probe photons and subsequently ionized by a third one. Such intermediate resonances have been observed before in fs-experiments using multiphoton schemes.[24,53,54] The time-dependence of the total photoelectron

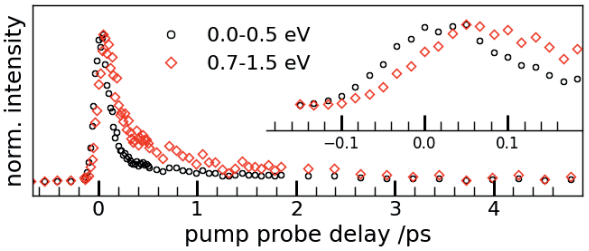

Fig. 8 Normalized decays of the bands at low (0.0-0.5 eV) and high (0.7-1.5 eV) electron kinetic energy. The inset shows a zoom of the decay at early times. The decays are normalized on the maximum.

signal is again depicted in the horizontal axis on top of the 2D map. In contrast to the spectrum at λ_{probe}=398 nm, a fit to the signal requires a biexponential function with two time constants for both peaks. In fig. 8 the decays for the two different peaks

are compared. The peak at higher energy has a slower rise-time and the second time-constant is longer. The two peaks cannot be completely separated, therefore only the total photoelectron signal fitted with a biexponential function is discussed. While for the first decay a time constant $\tau_1 = 70$ fs is found, similar to the value of 82 fs at λ_{probe}=398 nm within the error bars of the fit, the second time constant is much longer, $\tau_2 = 1.5$ ps. Concerning the photoelectron angular distribution, with 398 nm probe a positive anisotropy β_2 of 1.0 is found. The photoelectron spectrum with 798 nm also showed a positive anisotropy β_2 of about 1.0 over the complete band, but since interpretation of the photoelectron angular distribution in multiphoton ionization is challenging, it will not be considered in the following.

4.3 Excited states of the benzyl radical

Although the electronic structure of the benzyl radical has been studied before, there are still a number of open questions concerning the assignment of its excited states. The assignments available in the theoretical literature are mostly based on calculations that include only valence π-orbitals. Obviously, excited states built from 2pπ-orbitals antisymmetric to the molecular plane $\sigma(xz)$ can only belong to the A_2 and B_2 irreducible representations of the C_{2v} symmetry group. Bingel[55] initially assigned the states to the following irreducible representations (X=1 $^2B_2$, A=1 $^2A_2$, B=2 $^2B_2$, C=2 $^2A_2$ and $D = 3\ ^2B_2$) based on a Hückel calculation. Valence bond calculations by the same author lead to a different ordering of states.

More advanced configuration interaction calculations were performed by Kruglyak[56], who observed that depending on the type of excitations included the spectrum is distorted and the ordering of states changes. In order to provide a more reliable assignment we have performed CASSCF+MRCI calculations using previously described methodology (see Computational Methods). The excited states are listed together with their electronic character in Table 1. Our results show that the initially excited state in the experiment is either the 2 $^2A_2$ ($\pi\pi^*$) or the p_y-Rydberg state, which are almost degenerate and have by far the highest oscillator strengths among the neighboring states. The 2 $^2A_2$ state is flanked by two lower lying 3p$_{x,z}$-Rydberg states and a higher lying 3p$_y$ Rydberg state followed by an almost dark 4 $^2B_2$ state with the $\pi\pi^*$ character. Thus the experimentally observed D-band consists of several close lying states. The only bright electronic state close to the experimentally observed C-Band is the 1 $^2A_1$ s-Rydberg state located at 4.16 eV. However, the strong absorption peak in the ultraviolet spectrum of benzyl at 4.062 eV (C-state) and a weaker one at 2.728 eV (A-state) were previously both assigned to transitions to states of A_2 symmetry.[60] Ward[61], who measured and analysed the vibronic spectrum of the C-state (assigned to 2 $^2A_2$) found no apparent vibrational progressions. This was interpreted as a sign of a small geometry change between the ground and excited state minima. Finally, the two lowest two excited states 2 $^2B_2$ and 1 $^2A_2$ are almost degenerate. There has been some controversy about the ordering of these two states[62] (and references therein), with CASSCF π-space calculations[63] predicting them to be almost degenerate. The lowest state, be it 1 $^2A_2$ or 2 $^2B_2$, must be rather long-lived as fluorescence was observed from this state[62]. Experimentally the symmetry of an excitation can be deduced from photoselection rules[64]. By exciting different methylsubstituted benzyl radicals in a rigid solution with polarized light and measuring the polarized emission, Johnson[64] could determine the orientation of the transition dipole moment. The resulting experimental assignment (A or B = $^2B_2$, C=$^2B_2$, D=$^2A_2$) is at odds with MO theory. Since nonadiabatic dynamics simulations at the CASSCF-MRCI level are not feasible, we have performed a series of CASSCF calculations in order to determine the lowest possible level of theory which provides qualitatively the same ordering of states as in CASSCF-MRCI calculations. In Table 1 the performance of the cheaper CASSCF(7,8)/(6-31G*,s-Ryd) method is compared to the much more expensive SA-9-CASSCF(7,11)+MRCI/(aug-cc-pVDZ,s-,p-Ryd) method: Due to the lack of dynamic correlation the excitation energies are higher, but the s-Rydberg state is confirmed to lie below the $\pi\pi^*$-state. The oscillator strengths are not correct, since the basis set is too small.

State		CASSCF(7,11)+MRCI[a]		CASSCF(7,8)[b]	EOMCCSD[c]	Experimental
State	Sym.	E	Dominant config.	E	E	E
D_0	$1\,^2B_2$	0.0	$0.90\times(\pi_1)^2(\pi_2)^2(\pi_3)^2(\pi_4)^1$			X
D_1	$2\,^2B_2$	3.08 $(3\cdot10^{-3})$	$0.64\times(\pi_1)^2(\pi_2)^1(\pi_3)^2(\pi_4)^2$	3.06 $(1.5\cdot10^{-2})$	3.58 $(1.7\cdot10^{-3})$	A 2.728[i]
D_2	$1\,^2A_2$	3.09 (0.0)	$0.64\times(\pi_1)^2(\pi_2)^2(\pi_3)^2(\pi_5^*)^1$	3.20 $(5\cdot10^{-4})$	3.57 (0.0)	B 2.886[ii]
D_3	$1\,^2A_1$	4.16 $(2.5\cdot10^{-2})$	$0.91\times(\pi_1)^2(\pi_2)^2(\pi_3)^2(s)^1$	4.35 $(1.5\cdot10^{-3})$	4.65 $(4.1\cdot10^{-3})$	C 4.06[iii]
D_4	$2\,^2A_1$	4.65 $(3\cdot10^{-3})$	$0.91\times(\pi_1)^2(\pi_2)^2(\pi_3)^2(p_z)^1$			
D_5	$1\,^2B_1$	4.72 (0.0)	$0.92\times(\pi_1)^2(\pi_2)^2(\pi_3)^2(p_x)^1$			
D_6	$2\,^2A_2$	4.75 (0.24)	$0.64\times(\pi_1)^2(\pi_2)^2(\pi_3)^1(\pi_4)^2$	5.00 $(3\cdot10^{-4})$	4.67 $(4.7\cdot10^{-2})$	D 4.9[iv]
D_7	$3\,^2B_2$	4.76 (0.18)	$0.79\times(\pi_1)^2(\pi_2)^2(\pi_3)^2(p_y)^1$			
D_8	$4\,^2B_2$	4.89 $(3\cdot10^{-3})$	$0.65\times(\pi_1)^2(\pi_2)^2(\pi_3)^1(\pi_4)^1(\pi_5^*)^1$			
S_0	$1\,^1A_1$	6.61	$0.93\times(\pi_1)^2(\pi_2)^2(\pi_3)^2$			X^+ 7.24[v]

a) SA-9-CASSCF(7,11)+MRCI/(aug-cc-pVDZ, s-,p-Ryd) **b)** SA-5-CASSCF(7,8)/(6-31G*, s-Ryd) **c)** EOMCCSD/aug-cc-pVDZ i) ref.[13] ii) ref.[57] iii) ref.[14] iv) ref.[58] v) ref.[59]

Table 1 Excitation and ionization energies in eV, oscillator strengths in brackets.

4.4 Potential energy surfaces

The important points on the potential energy surfaces were characterized using the **SA-5-CASSCF(7,8)/(6-31G*,s-Ryd)** method as a compromise between accuracy and speed. To test whether the assignment of the *C*-state as the s-Rydberg state is a viable possibility, the geometry in $1\,^2A_1$ state was optimized. A metastable minimum exists that differs only be a slight contraction of the benzyl-ring along the C_2 axis. The wavepacket can thus in principle return several times to the excited state minimum giving rise to a vibrational progression as observed for the *C* state. This progression is not expected to be very pronounced as the geometric difference between the ground and $1\,^2A_1$ state minima is very small and the excited state has a finite lifetime. In Fig.9 the potential energy surfaces are scanned following a path from the Franck-Condon point to the minimal energy conical intersection (MECI) D_4/D_3, then to the MECI D_3/D_2 and to the MECI D_2/D_1. Only the bond lengths in the ring change in going from one conical intersection to the next and the molecule remains planar: At the conical intersection D_4/D_3 the bonds between the ortho- and meta-carbons are elongated; at the conical intersection D_3/D_2 the same bonds are shortened and at the conical intersection D_2/D_1 all bonds in the ring expand, while the bond to the CH_2 group shortens.

However, the planar geometry is distorted when the CI to the ground state is reached. The conical intersection between D_1 and D_0 lies at a ring-puckered geometry with elongated (or broken) bonds, which at the CASSCF-level with only π-electrons in the active space is very high in energy. Probably orbitals from the σ-framework would have to be included to describe this conical intersection accurately. However, in any case the aromatic nature of the benzyl radical will enforce planarity and shift this conical intersection to high energies. Therefore the D_1 state is expected to be long lived and if it deactivates after a long time through the conical intersection, the benzyl radical might break apart.

The energies of the conical intersections suggest that the lifetime of the s-Rydberg state should depend on the kinetic energy of the wavepacket. Starting at the Franck-Condon point, the wavepacket slides down the potential energy surface of the D_4 state and crosses the conical intersection to the s-Rydberg state D_3, where it remains trapped, since the conical intersection to D_2 lies much higher in energy. If the kinetic energy of the wavepacket increases, because a high vibrational state on D_4 is excited initially or because it drops down from higher excited states, the D_3/D_2 conical intersection becomes accessible.

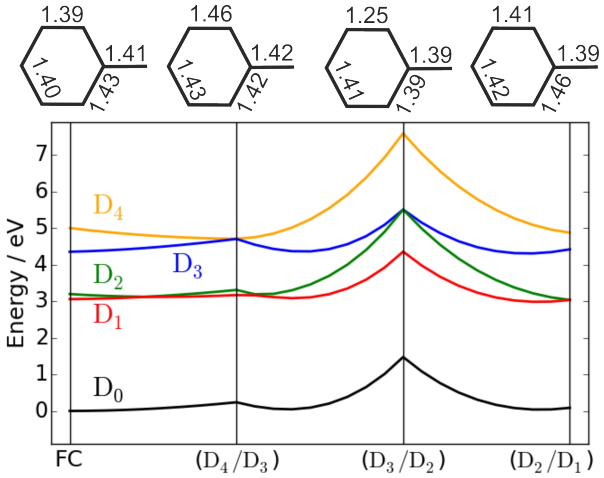

Fig. 9 SA-5-CASSCF(7,8)/(6-31G*,s-Ryd) potential energy scan from the Franck-Condon point (FC) to different conicial intersections. The intermediate geometries were interpolated linearly. The bond lengths (in Å) at the key geometries (minimum D_0, conical intersections (D_4/D_3), (D_3/D_2), (D_2/D_1)) are depicted above.

4.5 Non-adiabatic molecular dynamics with CASSCF(7,8)/(6-31G*,s-Rydberg)

Populations. Fig.10 a) depicts the adiabatic state populations averaged over all trajectories. Populations are obtained by counting the number of trajectories on an adiabatic state at each time step. It is important to stress, that the populations are adiabatic ones: The character of a state may change, even if the colour of the respective curve remains the same and vice versa. Inspection of the diagonal elements of the density matrices (see supplementary material for an example) shows that at time $t=0$ the adiabatic state D_3 has s-Rydberg and D_4 has $\pi-\pi^*$ character in the Franck-Condon region. One could be tempted to read off the graph that

the non-adiabatic transition from the $\pi-\pi^*$ to the s-Rydberg state takes place in a few fs. However, during the first 100 fs, both electronic states are energetically very close and cross without having the system jump from its inital state to the other one. Since in fig. 10a the populations of the state number are plotted as a function of time, the curves switch order when crossing (sometimes the $\pi-\pi^*$ state is higher in energy, sometimes the s-Rydberg) without changing the nature of the state. The resulting oscillations in the adiabatic populations are visible in the orange and blue curve in the first 100 fs. So the initially pumped state has partially $\pi-\pi^*$ and s-Rydberg character around the Franck-Condon region. After the first 100 fs the energy gap between the $\pi-\pi^*$ and the s-Rydberg states widens, so that from this point on it is justified to assign the D_3 population to the s-Rydberg state.

Eventually most trajectories end up in the D_1 ($1\ ^2A_2$) state, which is almost degenerate with D_2 ($2\ ^2B_2$). The small population on D_2 ($2\ ^2B_2$) is again due to the occasional flipping of the energetic order between D_1 ($1\ ^2A_2$) and D_2 ($2\ ^2B_2$). After the wavepacket drops to the first excited state, it remains there, since D_1 is separated by a large energetic gap from the ground state.

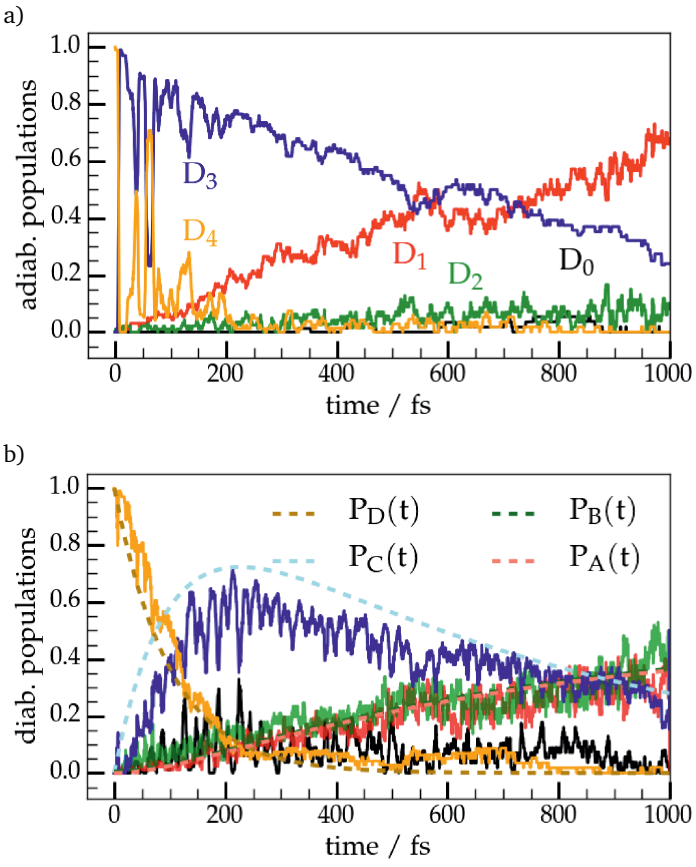

Fig. 10 a) Adiabatic state populations from non-adiabatic dynamics simulation with CASSCF(7,8)/(6-31G*,s-Rydberg) following vertical excitation to D_4 ($2\ ^2A_2$, $\pi-\pi*$). **b)** Diabatic populations based on the orbital occupations. A fit of the diabatic populations to rate equations involving the A/B band, the C band and the D band determines the lifetime of s-Rydberg (C) state to be $\tau \approx 700 \pm 100$ fs (dashed thin blue). The ground state population is an artifact of the diabatization method.

Lifetimes. The longer experimental time-constant $\tau_2 = 1.5$ ps refers to the lifetime of the s-Rydberg state, which is the one visible in the photoelectron spectrum recorded at 798 nm probe. Therefore we will focus on this lifetime. The deactivation of the s-Rydberg state can be described more clearly after defining "diabatic" states, whose characters remain constant. To perform a crude diabatization, the diagonal elements of the reduced density matrix were computed for the electronic wavefunction of the current adiabatic state along the trajectory. The fractional occupations of the active orbitals in the electronic wavefunction indicate its character ($\pi-\pi^*$ or s-Rydberg). The current state can then be related to a reference state at the Franck-Condon geometry having a similar orbital occupation. This procedure dinstinguishes between valence and Rydberg states but leads to ambiguities among valence states, since the occupation numbers can be identical for valence states built from excitations containing the same orbitals but having different relative phases.

The resulting trajectory populations on the diabatic states are shown in Fig.10 b). Assuming that transitions happen only between adjacent states, the following rate equations describe the populations of the A,B,C and D bands:

$$\frac{dP_D}{dt} = -\frac{1}{\tau_D}P_D(t) \quad (1)$$

$$\frac{dP_C}{dt} = \frac{1}{\tau_D}P_D(t) - \frac{1}{\tau_C}P_C(t) \quad (2)$$

$$\frac{dP_A}{dt} + \frac{dP_B}{dt} = \frac{1}{\tau_C}P_C(t) \quad (3)$$

where the lifetimes τ_C and τ_D of the $\pi-\pi^*$ (D) and s-Rydberg (C) states, respectively, are to be determined from a fit to the diabatic populations. Initially all trajectories start in the $\pi-\pi^*$ state, so $P_D(0) = 1$ and $P_{A,B,C}(0) = 0$. A manual fit to the solutions of the rate equations determines the time constants as $\tau_C = (700 \pm 100)$ fs and $\tau_D = (100 \pm 50)$ fs. The large error intervals account for the statistical fluctuations in the simulated population curves and the uncertainty in choosing the best fit by eye.

To fit the time-dependence of the experimental total photoelectron signal with 798 nm probe, two exponentials are required, one with a $\tau_1 = 70$ fs and a second one with $\tau_2 = 1.5$ ps. The short-lived component could be associated with initial transition from $2\ ^2A_2$ to the s-Rydberg state. The full complexity of this process is probably not accounted for in our dynamics simulation due to the incomplete description of the initially excited wavepacket. The pump pulse creates a superposition of the valence and p-Rydberg states in the D-band, since the stationary CASSCF+MRCI calculation showed that several p-Rydberg states lie in close proximity to the $\pi\pi^*$ state.

In the framework of surface hopping trajectories the creation of a complex initial wavepacket could be simulated in principle by including the pump pulse explicitely into the propagation of the electronic Schroedinger equation[65]. We did this for several initial geometries drawn randomly from the Wigner distribution: The electronic Schrödinger equation was propagated in the presence of a pump pulse having a Gaussian envelope of FWHM of 80 fs and a carrier frequency corresponding to 265 nm. The nuclei were frozen and the excitation energies and transition dipole moments (CASSCF(7,11)+MRCI level of theory) at the initial geom-

etry were used for all later time steps. The electronic population was transferred in some cases to the p-Rydberg states, in others to the $\pi - \pi^*$ state and sometimes excited states were only populated transiently during the duration of the pump pulse when no state was in resonance. This suggests that p-Rydberg states, which we did not include in the dynamics simulations to make the computations feasible, participate in the initial dynamics.

The photoelectron spectrum with 398 nm probe shows an intense and well defined peak, indicating diagonal Franck-Condon factors. The peak does not show any rotational anisotropy and its photoangular distribution is anisotropic. Based on the arguments outlined above this strong photoelectron signal that decays after ≈ 70 fs is in agreement with ionization from a p-Rydberg states. The long-lived component with $\tau_2 = 1.5$ ps can be assigned to the lifetime of the s-Rydberg state, in agreement with the computed lifetime $\tau_C = 700$ ps. The fact that the D_3 (s-Rydberg) state is rather long-lived is consistent with the observation of a vibrationally resolved spectrum by Ward[61] and Margraf et al.[16] after exciting the C state.

Deactivation mechanism. The non-adiabatic dynamics is not accompanied by large geometrical distortions. The aromatic π-system holds the benzyl radical in the planar configuration. Only a small puckering of the ortho-carbon is discernible. Deactivation through a conical intersection with a puckered ring has been observed in other aromatic molecules such as furan[66]. In most trajectories, however, reaching the conical intersections seams between the excited states requires only small changes in the aromatic bond lengths in the carbon ring. The adiabatic energies along a typical trajectory are shown in Fig. 11: Initially the energies of D_3 and D_4 oscillate around each other, until a gap opens between the two. As soon as a conical intersection is hit and the trajectory drops to a lower electronic state, the amplitudes of the energy oscillations increase strongly because of the additional kinetic energy deposited into the nuclear system.

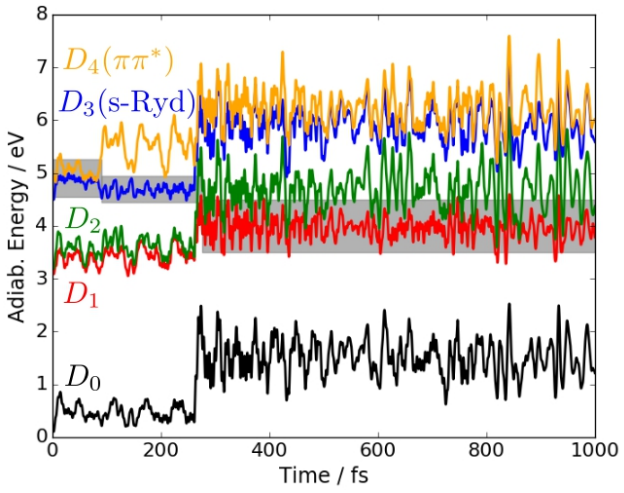

Fig. 11 Adiabatic energies along a typical trajectory. The current electronic state of the trajectory is highlighted by the grey areas.

5 Discussion

The spectrum of the 265 nm (4.68 eV) pump pulse overlaps with the lower edge of the D-band that contains several closely lying electronic states. According to the CASSCF+MRCI calculations, the brightest state in the D-band is the $\pi\pi^*$ state with symmetry 2 $^2A_2$ at 261 nm (4.75 eV), but at least the 3 $^2B_2$ $3p_y$ Rydberg state carries significant oscillator strength as well. Although the spectrum of the pump pulse reaches its maximum intensity at a slightly lower energy, the spectral width of a few nm ensures that there is still some spectral overlap with the 2 $^2A_2$ state. The remaining states in the D-band below the 2 $^2A_2$ state have zero oscillator strength.

At the D_0 minimum the 2 $^2A_2$ ($\pi\pi^*$) state has a larger oscillator strength than the Rydberg states, but Rydberg states in general exhibit a higher photoionization cross section and thus contribute strongly to the photoelectron spectrum. Therefore we conclude that mostly a $\pi\pi^*$ state is excited by the pump pulse, but that the contributions from one (or more) of the Rydberg states to the wavepacket dominate in the photoionization probe step. For photoionization with a single photon, Fermi's Golden Rule is applicable and the observed anisotropy of the photoelectron distribution carries information about the electronic character of the initial bound state. In particular s-like Rydberg states can be distinguished by a very high anistropy parameter $\beta \approx 2$. For two- or multiphoton ionization the photoelectron distribution is affected by the intermediate states in the probe step, so that we will refrain from the quantitative analysis of the photoangular distribution.

With a single photon of $\lambda_{\text{probe}} = 398$ nm (3.115 eV), assuming an ionization energy of IE $= 7.2$ eV, electronic states with excitation energies above 4.098 eV can be imaged. Ionizing from a p-Rydberg state in the D-band leads to a strong signal at a photoelectron kinetic energy of eKE ≈ 0.3 eV.

If the wavepacket reaches the C-state, which computationally is identified as the s-Rydberg state 1 $^2A_1$, the resulting peak in the photoelectron spectrum should be located around eKE $= 0.08$ eV. In fact contributions at low eKE are visible in the spectrum. These considerations hold for the Franck-Condon geometry. As the wavepacket spreads, ionization energies may shift.

The observed peak at eKE $= 0.3$ eV is associated with an anisotropy of $\beta \approx 1$ and at first glance might fit to the s-Rydberg C-state. On the other hand, the energetic position of the peak agrees more with one of the p-Rydberg states in the D-band. The observation of a single peak in the 398 nm probe spectrum indicates diagonal Franck-Condon factors in the probe step and thus supports assignment to an ion-like p-Rydberg state. The resolution of the photoelectron images originating from radicals is not sufficient to extract separate β-parameters for different energy regions without a doubt (see supporting material for the energy dependence of the β-parameter according to the Cooper-Zare formula). We therefore assign the peak at eKE $= 0.3$ in the one-photon ionization spectrum to ionisation from the p-Rydberg states surrounding the initially pumped 2 $^2A_2$ state and the time constant of $\tau_1 = 82$ fs to the depopulation of the states in the D-band to the lower C state. The time-trace of the total photoelectron signal (see top inset in Fig.5) for single photon ionization is fit with a single

exponential function. However, zooming into the time interval 200-800 fs shows that the curve flattens, so that a second exponential with a larger time constant could be hidden in the trace. This could be attributed to photoelectrons originating from the C state. The signal from the C state disappears quickly not because it is depopulated, but simple because the energy of a single photon is not sufficient to ionize the state.

The photoelectron spectra recorded with a 798 nm (1.554 eV) probe pulse are complementary to the single-photon experiment, since the combined energy of three photons (3×1.554 eV = 4.662 eV) is enough to ionize the C-state. On the downside multiphoton ionization complicates the analysis, because signals from ionization events with two or three photons are superimposed in the same energy region. Ionization with 2 photons from the D-band leaves the electrons with an energy of eKE $\leq$ 0.6 eV, while ionization with 3 photons from the D-band or the 1 $^2A_1$ state leads to vibrational progressions in the region below eKE = 2.2 eV or eKE = 1.6 eV, respectively. Indeed the photoelectron spectrum in Fig.6 exhibits multiple peaks in the range eKE $\approx 0.0 - 2.2$ eV. However, these peaks might originate from intermediate Rydberg resonances in the probe step. The time-trace of the total photoelectron signal matches a double-exponential decay. The short time-constant of $\tau_1 = 70$ fs agrees with the $\tau_D = 100$ fs needed for the population transfer from 2 $^2A_2$ to 1 $^2A_1$ in the molecular dynamics simulation. The longer time-constant of $\tau_2 = 1.5$ ps relates to the computed time-constant $\tau_C = 700$ fs for the depopulation of the 1 $^2A_1$ (C) state. We therefore conclude that the non-radiative deactivation of the benzyl radical proceeds via the following transitions:

$$D \xrightarrow{\tau_1 \approx 70\text{fs}} C \xrightarrow{\tau_2 \approx 1.5\text{ps}} A, B \quad (4)$$

Although the probe energy was not high enough to follow any further deactivation from the A or B states to the ground state, the simulation suggests that these states are long-lived in agreement with the pronounced vibrational structure observed in absorption spectra.

6 Conclusion

We investigated the fast deactivation of the benzyl radical after excitation at 265 nm by femtosecond time-resolved photoelectron spectroscopy employing one- and multiphoton ionization. With wavefunction-based electronic structure methods we identified several p-Rydberg states in the D-band and an s-Rydberg state that matches the energy of the C-state. Comparison of the observed time-dependence of the total photoelectron signal with the non-adiabatic dynamics simulation leads to the conclusion that the initially pumped D-band deactivates within 70-80 fs to the C-state, which in turn slowly decays within 1.5 ps to the long-lived lowest excited state. The benzyl radical remains planar throughout the non-radiative decay, since the relevant conical intersections are mediated by bond length changes in the aromatic ring.

7 Acknowledgements

This project has been funded by the German Science Foundation (DFG) under contract FI 575/8-2 and by the research training school GRK 2112. J. H. and R. M. gratefully acknowledge the financial support by the European Research Council (ERC) Consolidator grant DYNAMO (Grant Nr. 646737). We also acknowledge the support from the European Union's Horizon 2020 research and innovation programme under grant agreement no 654148 Laserlab-Europe." (In brief: support from Laserlab-Europe (EU-H2020 654148)). Travel support by the DAAD and by PHC program PROCOPE 2015 (Grant No. 32980XH) is gratefully acknowledged. The authors kindly thank Olivier Gobert, Michel Perdrix and Delphine Guillaumet for setting up and maintaining the SLIC/LUCA laser. LP acknowledge ANR11-EQPX0005-ATTOLAB for support.

References

1 D. Hrovat and W. T. Borden, *J. Phys. Chem.*, 1994, **98**(41), 10460–10464.
2 A. Alexiou and A. Williams, *Combust Flame*, 1996, **104**(1-2), 51–65.
3 G. da Silva, C.-C. Chen, and J. W. Bozzelli, *J. Phys. Chem. A*, 2007, **111**, 8663–8676.
4 M. Damm, F. Deckert, H. Hippler, and G. Rink, *Phys. Chem. Chem. Phys.*, 1999, **1**(1), 81–90.
5 U. Brand, H. Hippler, L. Lindemann, and J. Troe, *Journal of Physical Chemistry*, 1990, **94**(16), 6305–6316.
6 H. Hippler, C. Reihs, and J. Troe, *Z. phys. Chem. Neue Fol.*, 1990, **167**, 1–16.
7 K. Luther, K. Oum, K. Sekiguchi, and J. Troe, *Phys. Chem. Chem. Phys.*, 2004, **6**, 4133–4141.
8 G. C. Eiden, K.-T. Lu, J. Badenhoop, F. Weinhold, and J. C. Weisshaar, *J. Chem. Phys.*, 1996, **104**, 8886–8895.
9 J. D. Savee, J. Zador, P. Hemberger, B. Sztaray, A. Bodi, and D. L.Osborn, *Mol. Phys.*, 2015, **113**(15-16), 2217–2227.
10 M. Heaven, L. Dimauro, and T. Miller, *Chem. Phys. Lett.*, 1983, **95**(4-5), 347–351.
11 T. D. Lin, X.-Q. Tan, T. M. Cerny, J. M. Williamson, D. W. Cullin, and T. A. Miller, *Chem. Phys.*, 1992, **167**(1-2), 203–214.
12 G. C. Eiden and J. C. Weisshaar, *J. Chem. Phys.*, 1996, **104**, 8896–8912.
13 K. Tonokura and M. Koshi, *J. Phys. Chem. A*, 2003, **107**(22), 4457–4461.
14 B. Ward, *Spectrochim. Acta, A*, 1968, **A 24**(7), 813.
15 L. Grajcar and S. Leach, *J. Chim. Phys. PCB.*, 1964, **61**(11-2), 1523–1530.
16 M. Margraf, B. Noller, C. Schroter, T. Schultz, and I. Fischer, *J. Chem. Phys.*, 2010, **133**(7), 074304.
17 M. Zierhut, B. Noller, T. Schlutz, and I. Fischer, *J. Chem. Phys.*, 2005, **122**, 094302.
18 Y. Song, X. Zheng, M. Lucas, and J. Zhang, *Phys. Chem. Chem. Phys.*, 2011, **13**, 8296–8305.
19 G. de Silva, J. A. Cole, and J. W. Bozzelli, *J. Phys. Chem. A*, 2009, **113**, 6111–6120.
20 V. Blanchet, S. Lochbrunner, M. Schmitt, J. Shaffer, J. Larsen, M. Zgierski, T. Seideman, and A. Stolow, *Faraday Discuss.*,

2000, **115**, 33–48.
21 I. Fischer, M. Villeneuve, M. Vrakking, and A. Stolow, *J. Chem. Phys.*, 1995, **102**(13), 5566–5569.
22 A. Stolow, A. E. Bragg, and D. M. Neumark, *Chem. Rev.*, 2004, **104**(4), 1719–1157.
23 T. Suzuki, *Annu. Rev. Phys. Chem.*, 2006, **57**.
24 P. Hemberger., J. Kohler, I. Fischer, G. Piani, L. Poisson, and J. Mestdagh, *Phys. Chem. Chem. Phys.*, 2012, **14**(18), 6173–6178.
25 B. Noller, L. Poisson, R. Masimenka, I. Fischer, and J. Mestdagh, *J. Am. Chem. Soc.*, 2008, **130**(45), 14980.
26 B. Noller, R. Masimenka, I. Fischer., M. Armone, B. Engels, C. Alcaraz, L. Poisson, and J. Mestdagh, *J. Phys. Chem. A*, 2007, **111**(10), 1771–1779.
27 J. C. Tully, *J. Chem. Phys.*, 1990, **93**(2).
28 M. S. Schuurman, J. Giegerich, K. Pachner, D. Lang, B. Kiendl, R. J. MacDonell, A. Krueger, and I. Fischer, *Chem. Eur. J.*, 2015, **21**, 14486–14495.
29 J. Giegerich, J. Petersen, R. Mitrić, and I. Fischer, *Phys. Chem. Chem. Phys.*, 2014, **16**(13), 6294–6302.
30 A. Röder, K. Issler, L. Poisson, A. Humeniuk, M. Wohlgemuth, M. Comte, F. Lepetit, I. Fischer, R. Mitrić, and J. Petersen, *J. Chem. Phys.*, 2017.
31 D. W. Kohn, H. Clauberg, and P. Chen, *Rev. Sci. Instrum.*, 1992, **63**, 4003 – 4005.
32 M. Gasser, J. A. Frey, J. M. Hostettler, and A. Bach, *Chem. Comm.*, 2011, **47**, 301–303.
33 A. T. B. Eppink and D. H. Parker, *Rev. Sci. Instrum.*, 1997, **68**(9), 3477–3484.
34 E. Gloaguen, J. M. Mestdagh, L. Poisson, F. Lepetit, J. Visticot, B. Soep, M. Coroiu, A. Eppink, and D. H. Parker, *J. Am. Chem. Soc.*, 2005, **127**(47), 16529–16634.
35 G. A. Garcia, L. Nahon, and I. Powis, *Rev. Sci. Instrum.*, 2004, **75**(11), 4990–4996.
36 M. J. Frisch, G. W. Trucks, H. B. Schlegel, G. E. Scuseria, M. A. Robb, J. R. Cheeseman, G. Scalmani, V. Barone, B. Mennucci, G. A. Petersson, H. Nakatsuji, M. Caricato, X. Li, H. P. Hratchian, A. F. Izmaylov, J. Bloino, G. Zheng, J. L. Sonnenberg, M. Hada, M. Ehara, K. Toyota, R. Fukuda, J. Hasegawa, M. Ishida, T. Nakajima, Y. Honda, O. Kitao, H. Nakai, T. Vreven, J. A. Montgomery, Jr., J. E. Peralta, F. Ogliaro, M. Bearpark, J. J. Heyd, E. Brothers, K. N. Kudin, V. N. Staroverov, R. Kobayashi, J. Normand, K. Raghavachari, A. Rendell, J. C. Burant, S. S. Iyengar, J. Tomasi, M. Cossi, N. Rega, J. M. Millam, M. Klene, J. E. Knox, J. B. Cross, V. Bakken, C. Adamo, J. Jaramillo, R. Gomperts, R. E. Stratmann, O. Yazyev, A. J. Austin, R. Cammi, C. Pomelli, J. W. Ochterski, R. L. Martin, K. Morokuma, V. G. Zakrzewski, G. A. Voth, P. Salvador, J. J. Dannenberg, S. Dapprich, A. D. Daniels, Ö. Farkas, J. B. Foresman, J. V. Ortiz, J. Cioslowski, and D. J. Fox, Gaussian09 Revision E.01.
37 P. Perdew, K. Burke, and M. Ernzerhof, *Phys. Rev. Lett.*, 1996, **77**, 3865–3868.
38 C. Adamo and V. Barone, *J. Chem. Phys.*, 1998, **13**, 6158–6170.
39 H. Iikura, T. Tsuneda, T. Yanai, and K. Hirao, *J. Chem. Phys.*, 2001, **115**, 3540–3544.
40 A. Becke, *J. Chem. Phys.*, 1993, **98**, 5648–5652.
41 C. Lee, W. Yang, and R. Parr, *Phys. Rev. B*, 1988, **37**, 785–789.
42 T. Yanai, D. Tew, and N. Handy, *Chem. Phys. Lett.*, 2004, **393**, 51–57.
43 J. Chai and M. Head-Gordon, *J. Chem. Phys.*, 2008, **128**, 084106.
44 K. Kaufmann, W. Baumeister, and M. Jungen, *J. Phys. B: At. Mol. Opt. Phys.*, 1989, **22**, 2223–2240.
45 H.-J. Werner, P. J. Knowles, G. Knizia, F. R. Manby, and M. Schütz, *WIREs Comput Mol Sci*, 2012, **2**, 242–253.
46 R. Krishnan, J. Binkley, R. Seeger, and J. Pople, *J. Chem. Phys.*, 1980, **72**, 650–654.
47 P. Lisinetskaya and R. Mitrić, *Phys. Rev. A*, 2011, **83**, 033408.
48 J. Tully, *J. Chem. Phys.*, 1990, **93**, 1061.
49 G. Granucci, M. Persico, and A. Toniolo, *J. Chem. Phys.*, 2001, **114**, 10608–10615.
50 R. Mitrić, U. Werner, M. Wohlgemuth, G. Seifert, and V. Bonačić-Koutecký, *J. Phys. Chem. A*, 2009, **113**, 12700–12705.
51 G. da Silva, C.-C. Chen, and J. W. Bozzelli, *J. Am. Chem. Soc.*, 2006, **128**, 3169–3178.
52 V. Blanchet, M. Z. Zgierski, T. Seideman, and A. Stolow, *Nature*, 1999, **401**, 52–54.
53 M. Tsubouchi and T. Suzuki, *J. Phys. Chem. A*, 2003, **107**, 10897–10903.
54 C. Schick and P. M. Weber, *J. Phys. Chem. A*, 2001, **105**, 3725–3734.
55 W. Bingel, *Z. Naturforschg.*, 1955, **10a**, 462.
56 Y. Kruglyak and E. Mozdor, *Theoret.chim.Acta*, 1969, **15**, 374–384.
57 F. Negri, G. Orlandi, F. Zerbetto, and M. Z. Zgierski, *J. Chem. Phys.*, 1990, **93**, 600–608.
58 F. Bayrakçeken, *Spectrochim. Acta A*, 2007, **68**, 143–146.
59 G. Eiden and J. Weisshaar, *J. Phys. Chem.*, 1991, **95**, 6194–6197.
60 E. Hedaya and D. McNeil, *J. Am. Chem. Soc.*, 1967, **89**, 4214–4216.
61 B. Ward, *Spectrochimica Acta*, 1967, **24A**, 813–818.
62 V. Smirnov and V. Plotnikov, *Uspekhi Khimii*, 1986, **55**, 1633–1666.
63 J. Rice, N. Handy, and P. Knowles, *J. Chem. Soc., Faraday Trans. 2*, 1987, **83**, 1643–1649.
64 P. Johnson and A. Albrecht, *J. Chem. Phys.*, 1968, **48**, 851–865.
65 R. Mitrić, J. Petersen, and V. Bonačić-Koutecký, *Phys. Rev. A*, 2009, **79**, 053416.
66 A. Humeniuk, M. Wohlgemuth, T. Suzuki, and R. Mitrić, *J. Chem. Phys.*, 2013, **139**, 134104.